




## ORIGINAL ARTICLE

# Molecular pathophysiology of human MICU1 deficiency

Nicolai Kohlschmidt<sup>1</sup> | Miriam Elbracht<sup>2</sup> | Artur Czech<sup>3</sup> | Martin Häusler<sup>4</sup> |  
 Vietxuan Phan<sup>3</sup> | Ana Töpf<sup>5</sup> | Kai-Ting Huang<sup>6</sup> | Adam Bartok<sup>6</sup>  | Katja Eggermann<sup>2</sup> |  
 Stephanie Zippel<sup>7</sup> | Thomas Eggermann<sup>2</sup> | Erik Freier<sup>3</sup>  | Claudia Groß<sup>1</sup> |  
 Hanns Lochmüller<sup>8,9,10,11</sup> | Rita Horvath<sup>12</sup> | György Hajnóczy<sup>6</sup> | Joachim Weis<sup>13</sup> |  
 Andreas Roos<sup>14</sup> 

<sup>1</sup>Institute of Clinical Genetics and Tumour Genetics, Bonn, Germany<sup>2</sup>Institute of Human Genetics, RWTH Aachen University Hospital, Aachen, Germany<sup>3</sup>Leibniz-Institut für Analytische Wissenschaften - ISAS - e.V, Dortmund, Germany<sup>4</sup>Division of Neuropediatrics and Social Pediatrics, Department of Pediatrics, RWTH Aachen University Hospital, Aachen, Germany<sup>5</sup>Institute of Genetic Medicine, International Centre for Life, Central Parkway, Newcastle upon Tyne, UK<sup>6</sup>MitoCare Center, Department of Pathology, Anatomy and Cell Biology, Thomas Jefferson University, Philadelphia, PA, USA<sup>7</sup>Centre for Social Pediatrics Mechernich, Mechernich, Germany<sup>8</sup>Department of Neuropediatrics and Muscle Disorders, Medical Center - University of Freiburg, Faculty of Medicine, Freiburg, Germany<sup>9</sup>Centro Nacional de Análisis Genómico, Center for Genomic Regulation, Barcelona Institute of Science and Technology, Barcelona, Spain<sup>10</sup>Children's Hospital of Eastern Ontario Research Institute, University of Ottawa, Ottawa, ON, Canada<sup>11</sup>Division of Neurology, Department of Medicine, The Ottawa Hospital, Ottawa, Ontario, Canada<sup>12</sup>Department of Clinical Neuroscience, University of Cambridge, Cambridge, UK<sup>13</sup>Institute of Neuropathology, RWTH Aachen University Hospital, Aachen, Germany<sup>14</sup>Department of Neuropediatrics, Centre for Neuromuscular Disorders in Children, University Hospital Essen, University of Duisburg-Essen, Essen, Germany**Correspondence**

Andreas Roos, Department of Neuropediatrics, Centre for Neuromuscular Disorders in Children, University Hospital Essen, University of Duisburg-Essen, 45122 Essen, Germany.  
 Email: andreas.roos@uk-essen.de

**Funding information**

Wellcome Trust, Grant/Award Number: 109915/Z/15/Z; Medical Research Council UK, Grant/Award Number: MR/N025431/1; European Regional Development Fund, Grant/Award Number: NME-GPS; Center for Scientific Review, Grant/Award Number: GM102724; European Research Council, Grant/Award Number: 309548; Ministerium für Innovation, Wissenschaft und Forschung des Landes Nordrhein-Westfalen; Newton Fund, Grant/Award Number: MR/N027302/1; Bundesministerium für Bildung und Forschung; European Community's Seventh Framework Programme, Grant/

**Abstract**

**Aims:** *MICU1* encodes the gatekeeper of the mitochondrial Ca<sup>2+</sup> uniporter, *MICU1* and biallelic loss-of-function mutations cause a complex, neuromuscular disorder in children. Although the role of the protein is well understood, the precise molecular pathophysiology leading to this neuropaediatric phenotype has not been fully elucidated. Here we aimed to obtain novel insights into *MICU1* pathophysiology.

**Methods:** Molecular genetic studies along with proteomic profiling, electron-, light- and Coherent anti-Stokes Raman scattering microscopy and immuno-based studies of protein abundances and Ca<sup>2+</sup> transport studies were employed to examine the pathophysiology of *MICU1* deficiency in humans.

**Results:** We describe two patients carrying *MICU1* mutations, two nonsense (c.52C>T; p.(Arg18\*) and c.553C>T; p.(Arg185\*)) and an intragenic exon 2-deletion presenting with ataxia, developmental delay and early onset myopathy, clinodactyly, attention deficits, insomnia and impaired cognitive pain perception. Muscle biopsies revealed signs of dystrophy and neurogenic atrophy, severe mitochondrial perturbations, altered Golgi structure, vacuoles and altered lipid homeostasis. Comparative mitochondrial Ca<sup>2+</sup> transport and proteomic studies on lymphoblastoid cells revealed that the [Ca<sup>2+</sup>] threshold and the

Nicolai Kohlschmidt, Miriam Elbracht, and Artur Czech are contributed equally to this work.

The work described has been carried out in accordance with the Code of Ethics of the World Medical Association (Declaration of Helsinki).

This is an open access article under the terms of the Creative Commons Attribution License, which permits use, distribution and reproduction in any medium, provided the original work is properly cited.

© 2021 The Authors. *Neuropathology and Applied Neurobiology* published by John Wiley & Sons Ltd on behalf of British Neuropathological Society.

Award Number: 2012-305121; AFM-Téléthon, Grant/Award Number: 21466

cooperative activation of mitochondrial  $\text{Ca}^{2+}$  uptake were lost in MICU1-deficient cells and that 39 proteins were altered in abundance. Several of those proteins are linked to mitochondrial dysfunction and/or perturbed  $\text{Ca}^{2+}$  homeostasis, also impacting on regular cytoskeleton (affecting Spectrin) and Golgi architecture, as well as cellular survival mechanisms.

**Conclusions:** Our findings (i) link dysregulation of mitochondrial  $\text{Ca}^{2+}$  uptake with muscle pathology (including perturbed lipid homeostasis and ER–Golgi morphology), (ii) support the concept of a functional interplay of ER–Golgi and mitochondria in lipid homeostasis and (iii) reveal the vulnerability of the cellular proteome as part of the MICU1-related pathophysiology.

#### KEYWORDS

Mitochondrial degeneration, lymphoblastoid cell proteomics, Spectrin, metabolic diseases, mitochondrial myopathy

## INTRODUCTION

Mitochondrial disorders are genetically heterogeneous and normally manifest as multisystem diseases with very heterogeneous clinical presentations based on the underlying molecular defect. Many syndromes caused by mutations affecting mitochondrial proteins are associated with a vulnerability of skeletal muscle, in addition to the nervous and ocular system. Mitochondrial diseases associated with myopathies are progressive disorders that produce significant disabilities and may cause premature death. However, within the clinical spectrum of multisystem mitochondrial diseases, the muscular phenotype may be outweighed by other clinical aspects such as neurodegeneration [1].

The mitochondrial  $\text{Ca}^{2+}$  uptake protein 1 (MICU1), encoded by the *MICU1* gene is the primary  $\text{Ca}^{2+}$ -sensing regulator of the pore of the mitochondrial  $\text{Ca}^{2+}$  uniporter formed by the mitochondrial calcium uniporter protein (MCU) and Essential MCU regulator (EMRE) [2–4]. Loss-of-function mutations in the *MICU1* gene cause an early onset multisystem disease characterised by proximal myopathy, learning difficulties and a progressive extrapyramidal movement disorder (OMIM #615673) [5]. *MICU1*<sup>(-/-)</sup> mice either die at birth, likely because of impaired neuronal respiratory control, [6] or are viable but manifest marked ataxia and muscle weakness [7]. At the cellular level, mitochondrial  $\text{Ca}^{2+}$  overload, resulting in altered mitochondrial morphology, reduced ATP-level and increased vulnerability to stress-induced cell death were documented [6,7]. In vitro studies of the functional consequences of *MICU1* mutations in patient-derived fibroblasts showed mitochondrial fragmentation related to altered  $\text{Ca}^{2+}$ -induced phosphorylation of DRP1 that initiates fission [8] and influences both cell survival and apoptosis. Thus, it has been assumed that MICU1 serves as a signal-noise discriminator in mitochondrial  $\text{Ca}^{2+}$  signalling that controls oxidative phosphorylation [9], a process of importance in tissues with dynamic energetic demands such as brain and skeletal muscle.

Although altered cellular  $\text{Ca}^{2+}$  homeostasis may impact on proper protein function and abundance, as well as on lipid homeostasis, the

overall cellular protein and lipid composition in human MICU1-deficient cells or tissues has not been studied yet. Thus, we aimed to explore the biochemical consequences of MICU1 deficiency in patient-derived cells and muscle tissue. We report two patients with biallelic *MICU1* mutations. In a patient-derived lymphoblastoid cell line, the lack of MICU1 protein and MICU1-deficient mitochondrial  $\text{Ca}^{2+}$  transport phenotype were validated. Label-free proteomic profiling was carried out and findings obtained in cells correlated with the morphological and biochemical perturbations detected by subsequent studies including light, electron and Coherent anti-Stokes Raman scattering (CARS) microscopy on the patient-derived muscle biopsies. Our study provides insights into myopathological and biochemical effects downstream of perturbed cellular  $\text{Ca}^{2+}$  homeostasis including an impact on Spectrin abundance and distribution as well as on lipid accumulation.

## MATERIALS AND METHODS

### Molecular genetics

Blood genomic DNA from index patient 1 was subjected to whole genome sequencing by deCODE Genetics (Iceland) using the TruSeq PCR-free library preparation kits from Illumina. Sequencing libraries were clustered to the surface of paired-end (PE) HiSeq X version 2.5 flowcells, using the Illumina cBot™ instrument. Each library was hybridised to a single lane on a flowcell, yielding in general >30X sequence coverage. Real-time analysis involved conversion of image data to base calling. Alignment to the human reference sequence (hg19) and variant calling were carried out using Burrows–Wheeler Aligner (BWA; <http://bio-bwa.sourceforge.net/>) and Genome Analysis ToolKit (GATK; <https://software.broadinstitute.org/gatk/>); variant call set was uploaded onto a proprietary genomics analysis platform (<https://www.wuxunextcode.com>). We sought recessive variants (i.e. homozygous and compound heterozygous) that were rare in the control population (MAF ≤1% <http://exac.broadinstitute.org/>) and had an impact on the protein structure (moderate to high Ensembl Variant Effect Predictor

(VEP). Sanger sequencing was used to confirm the identified *MICU1* variant and segregate it in the available family members.

A custom-designed Illumina Enrichment Kit was used to capture the genes under investigation in index patient 2. The generated library was sequenced on a MiSeq sequencer (Illumina). The generation of the analysed 'bam' or 'FastQ' files was carried out with the MiSeqReporter Software (v.2.6.2, Illumina, reference genome: hg19). Generated raw data were analysed using the SeqNext module of the SeqPatient software (JSI, v.4.3.0-B503). Approximately 99% of the target regions of interest (ROI) were covered with a coverage of >30X.

Uniparental disomy for chromosome 10 (upd [10]) was excluded in index patient 2 by microsatellite analysis of highly polymorphic markers located on chromosome 10. A list of markers used may be provided upon request.

### Analysis of copy numbers of exons encoding *MICU1*

Copy number variants of exons 1, 2 and 3, covering the presumed rearrangement of the *MICU1* gene (NM\_006077), were analysed in the DNA of patient 2 and his parents using qPCR. The respective qPCR primer sequences and conditions are available upon request. For the detection of larger genomic imbalances, the CytoScan® HD Array (Affymetrix, Santa Clara/CA, USA) was applied. Only CNVs >50 kb with a mean marker distance of <5 kb were considered.

### Generation of a lymphoblastoid cell line

Lymphoblastoid cell lines were generated from peripheral blood samples derived from the index patient and the healthy sibling as described previously.[10]

### Measurements of mitochondrial $\text{Ca}^{2+}$ uptake in permeabilised lymphoblasts

Fluorometric measurements of cytosolic  $[\text{Ca}^{2+}]_c$  were performed as previously described [2]. Briefly, saponin-permeabilised lymphoblasts (2.4 mg) were resuspended in 1.5 mL of intracellular medium containing 120 mM KCl, 10 mM NaCl, 1 mM  $\text{KH}_2\text{PO}_4$ , 20 mM Tris-HEPES at pH 7.2 and supplemented with proteases inhibitors (leupeptin, antipain, pepstatin, 1 mg/ml each), 2 mM MgATP, 2  $\mu\text{M}$  thapsigargin (Enzo) and maintained in a stirred thermostated cuvette at 35 °C. Assays were performed in presence of 20  $\mu\text{M}$  CGP-37157 (Enzo) and 1 mM succinate using a multiwavelength-excitation dual-wavelength-emission fluorimeter (DeltaRAM, PTI). The extramitochondrial  $\text{Ca}^{2+}$  concentration  $[\text{Ca}^{2+}]_e$  was assessed using the ratiometric  $\text{Ca}^{2+}$  probe Fura2-FA (1.5  $\mu\text{M}$ , Teflabs) or Fura-IoAff (formerly Fura-FF) (1  $\mu\text{M}$ , Teflabs). Fura fluorescence was recorded simultaneously using 340–380 nm excitation and 500 nm emission. Calibration of the Fura signal was carried out at the end of each measurement, adding 1 mM  $\text{CaCl}_2$ , followed by 10 mM EGTA/Tris, pH 8.5.

### Immunoblotting of *MICU1* and EMRE in lymphoblastoid cells

Western blotting of the permeabilised lymphoblast cells was carried out as described before [11].

### Proteomic profiling

As proteomic profiling is a powerful tool to obtain unbiased insights into pathophysiological processes, label-free protein quantification utilising liquid chromatography coupled to tandem mass spectrometry has been carried out on lymphoblastoid cells derived from one *MICU1* patient and his healthy sibling (as control). For further details see Data S1.

### Light, fluorescence and electron microscopy of patient-derived muscle biopsy

Seven-micrometre-thick sections were cut from cryopreserved muscle biopsy tissue. These sections were used for H&E staining and for enzyme histochemistry (NADH, ATPase, COX-SDH) as well as for immunofluorescence (IF). Fluorescence studies were carried out as described previously [12]. Light and electron microscopic investigations of the patient-derived muscle biopsy were carried out as described previously [12,13]. Further immunological studies were performed on 7- $\mu\text{m}$ -thick sections cut from muscle biopsy tissue fixed in formalin and embedded in paraffin. Primary antibodies used are as follows: *MICU1* (Abcam; dilution 1:100), POC1A (Sigma; dilution 1:100), STX5 (Thermo Fisher; dilution 1:100), GRP94 (Genetex; dilution 1:100), BiP (Genetex; dilution 1:100), CALR (Genetex, dilution 1:100), BSCL2 (Cell Signalling; dilution 1:100), LC-3 (Abcam; dilution 1:100), LAMP1 (Genetex; dilution 1:100), CASP1 (Santa Cruz; dilution 1:100), CytC (Santa Cruz; dilution 1:100), ACTN3 (Genetex; dilution 1:100) and ITGB4 (Millipore; dilution 1:100). Peroxidase-labelled secondary goat anti-rabbit and goat anti-mouse immunoglobulin antiserum (1:200, DCS, Hamburg, Germany) and diaminobenzidine (DAKO, USA) were used to detect antibody binding. Cellular structures were counter-stained with haematoxylin.

### Coherent anti-Stokes Raman scattering and Second Harmonic Generation spectroscopy, non-linear unmixing and statistical evaluation of muscle fibre calibres

CARS and second harmonic generation (SHG) measurements were performed on a modified Leica TCS SP8 CARS with an APE pico-Emerald laser system. Five-micrometre-thick sections were cut from FFPE tissue blocks and thoroughly deparaffinated. No further sample preparation was applied.

Non-linear unmixing of CARS data was performed as described previously [14] and the statistical evaluation was done on the basis

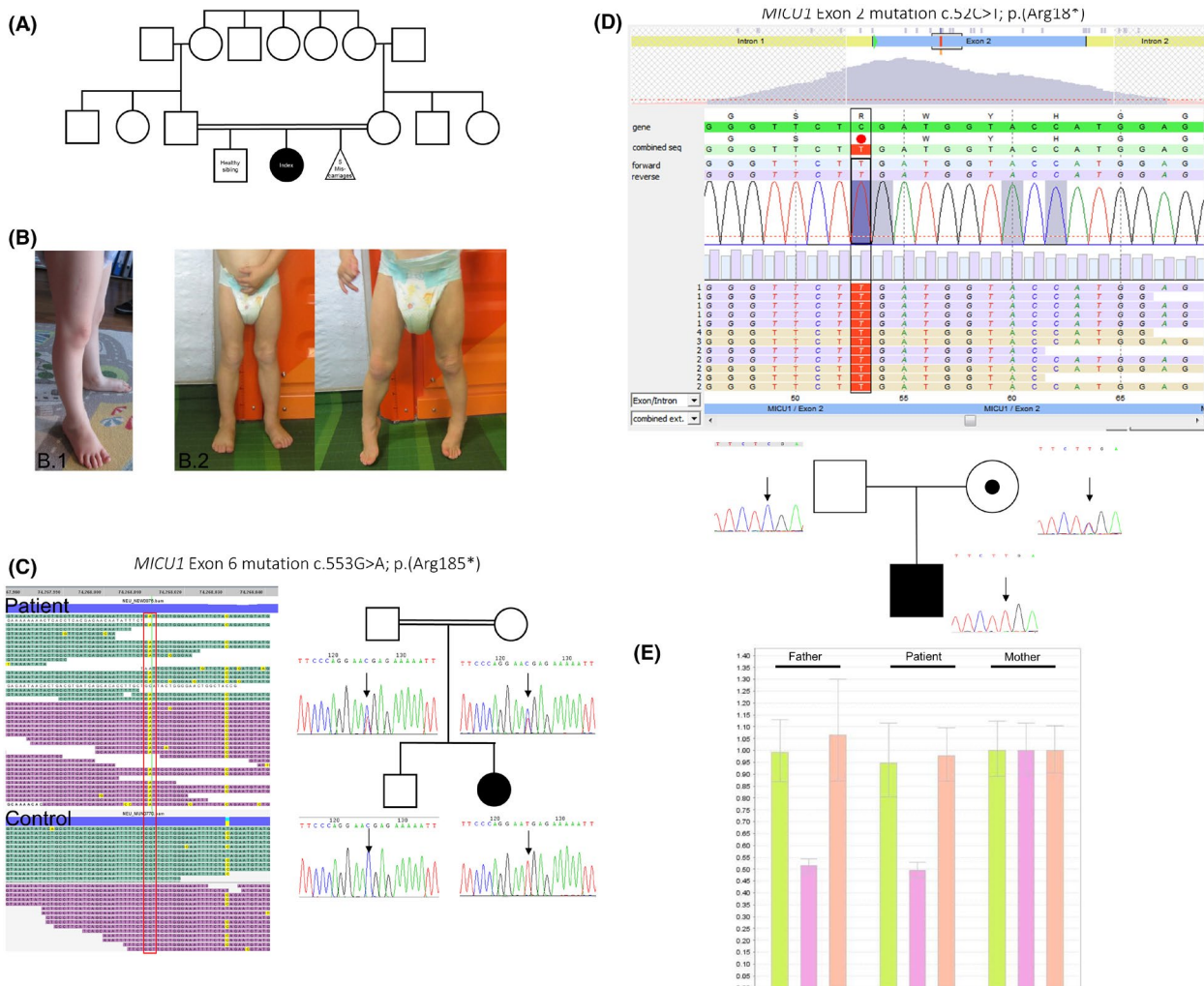


**FIGURE 1** Clinical and genetic data of the *MICU1* patients. (A) Family pedigree of index patient 1 showing the occurrence of five miscarriages. (B) Presentation of musculature in both index patients: loss of muscle mass in index patient 1 at the age of 36 months (B1). Pseudo-hypertrophy of calf muscles and tiptoes as preferred positioning of the legs in index patient 2 at the age of 32 months (B2). (C & D) Results of next generation sequencing (NGS) studies in both index patients: (C) genome sequencing studies in index case 1 identified a homozygous chr10: 74268012G>A change in the *MICU1* gene (upper left panel). This mutation is absent in the DNA sample of a control sample (lower left panel). Sanger sequencing-based segregation studies revealed heterozygosity for the mutation in both consanguineous parents and confirmed the homozygous presence in the DNA sample of index patient 1 (black arrows in right panel). (D) Results of NGS-based studies of exons and exon-intron boundaries revealed homozygosity for a sequence variant in exon 2 of the *MICU1* gene (chr10: 74268012; c.52C>T, p.(Arg18\*)) which was considered as likely pathogenic (class IV variant; upper panel). Sanger-based segregation studies confirmed homozygosity for the same mutation in the index patient but showed heterozygosity only in the mother (black arrows in lower panel). (E) Further qPCR showed a deletion of *MICU1* exon 2 in the patient and his father, whereas the adjacent exons 1 and 3 presented with two copies respectively. Quantitative PCR studies of *MICU1* exons 1–3 in the mother revealed normal results

of the CARS images (69 CARS measurements and 3380 muscle fibres in total).

For further details see Data S1.

**Immunoblot studies on whole muscle protein extracts**

SDS-PAGE and subsequent western blot studies on whole protein extracts from patient-derived muscle biopsies have been carried out

as described previously [15]. Primary antibodies against  $\beta$ -Spectrin (Novo Castra/Leica; # NCL-SPEC1; dilution 1:500), Tubulin (Sigma, # T5168; dilution 1:1000), Myotilin (Novo Castra/Leica; # NCL-MYOTILIN; dilution 1:10000), Dystrophin (Novo Castra/Leica; # NCL-DYS3; dilution 1:1000), Desmin (Novo Castra/Leica; # NCL-DES-DERII; dilution 1:1000),  $\beta$ -Dystroglycan (Novo Castra/Leica; # NCL-b-DG; dilution 1:1000) and  $\alpha$ -,  $\beta$ - and  $\gamma$ -Sarcoglycan (Novo Castra/Leica; # NCL-a-SARC/ NCL-b-SARC/ NCL-g-SARC; respective dilutions 1:1000) have been used.



## RESULTS

### Clinical presentation of the patients

The index patient was a girl, born as the first child of Turkish consanguineous parents (Figure 1A) after an uneventful pregnancy (parents had five prior miscarriages; Figure 1A). Whereas development of free walking was observed at age 18 months, speech development was delayed with her first words occurring at age 24 months and first sentences, at age 4 years. At this time, she showed normal tendon reflexes, normal muscle strength, moderate ataxia with frequent falls and reduced physical endurance. Chorea, dystonia, nystagmus or vitiligo were not recorded. She further showed extensive motor restlessness with reduced attention and a sleep disorder with frequent awakenings at night. At the age of 5 years, at last follow-up, she had improved showing normal physical endurance, improved sleep patterns, improved fine motor skills and markedly improved ataxic gait pattern. The parents, however, reported episodes of unsteady gait and reduced mobility which they attributed to lower limb pain. Slightly reduced global muscle strength, proximal muscular hypotonia, lumbosacral hyperlordosis and clinodactyly of the fifth fingers were noted (Figure 1B). Cognitive testing was in line with marked cognitive impairment. Electroencephalography and brain MRI studies proved normal. Serum creatine kinase (CK) levels were repeatedly elevated ranging from 3000 to 5500 U/l. Genetic testing including karyotyping, CGH-array, *FMR1*, *DMPK*, *FXN* and *SMN1* as well as screening for Prader-Willi syndrome gave normal results. The father was suffering from a progressive optic atrophy (visual acuity right =5%, left =20%), which could not be detected in our index patient. However, the reason for this clinical feature in the father has not been pursued.

The second patient is a previously healthy boy who at the age of 22 months, in the course of an acute upper respiratory tract infection, suddenly developed acute ataxia which spontaneously regressed within 2 days. Laboratory studies revealed an elevated CK value of 10,000 U/l which persisted during follow-up. At the age of 32 months, when he first presented to our hospital, he showed bilateral enlargement of the calf muscles, normal tendon reflexes, grossly normal muscle strength with no Gower's sign and normal ability to climb stairs. He tended to walk on tiptoes, although no fixed pointed foot was present. At age 40 months, the parents reported he had an impaired sensitivity to pain and an increased tendency to fall, possibly related to a marked motor restlessness combined with persistent pointed foot. This restlessness combined with reduced attention was still noted at age 4 years. At the age of 5 years, at last follow-up, there was no Gower's sign but moderate proximal weakness with reduced exercise capacity attributed to exercise-related proximal muscle pain. Electro- and echocardiography proved normal.

### Genetic testing

Whole genome sequencing of index patient 1 revealed a homozygous G > A change within the coding region of the *MICU1* gene

on chromosome 10 (chr10: 74268012; c.553C>T; exon 6 of 12; Figure 1C). This nucleotide change results in a premature stop codon at amino acid position 185 p.(Arg185\*), which has been described previously as being a pathogenic founder mutation in 13 patients from the Middle East [16]. This homozygous mutation is expected to lead to deficiency of the *MICU1* protein, which was validated in the immortalised lymphoblastoid cells by immunoblotting (Figure 6B) and highly likely to be responsible for the disorder manifesting in the index patient. Segregation of the mutation in the family could be demonstrated (Figure 1C).

In patient 2, next generation sequencing (NGS)-based testing of myopathy genes using an Illumina enrichment kit revealed homozygosity for a sequence variant in exon 2 of the *MICU1* gene (chr10: 74268012; c.52C>T, p.(Arg18\*)) which was considered as likely pathogenic (class IV variant) (Figure 1D). No further pathogenic sequence variants were detected in the regions of interest. The applied NGS-based approach did not allow the distinction between homozygosity of the sequence variant, compound heterozygosity for the variant and a deletion overlapping the region of interest, or a uniparental isodisomy of chromosome 10. However, uniparental disomy of chromosome 10 was excluded by using chromosome 10-specific microsatellite markers. Using qPCR, we could show that the patient carries a heterozygous deletion comprising exon 2 of the *MICU1* gene; exons 1 and 3 of the *MICU1* gene are not deleted (Figure 1E). The exact size of the deletion was not determined, and SNP array analysis failed to detect this relatively small deletion. Analysis of parental blood samples revealed that the mother is a heterozygous carrier of the c.52C>T (p.(Arg18\*)) sequence variant, whereas the deletion is of paternal origin (Figure 1D,E). The patient is therefore compound heterozygous for two loss-of-function variants in the *MICU1* gene.

### Biopsy findings

Muscle histology including H&E, NADH, COX-SDH, ATPase and toluidine blue staining showed fibre calibre variation, occasionally internalised myonuclei, fibre-type grouping, groups of lesioned basophilic fibres, focally increased NADH-labelling consistent with irregular focal accumulation of mitochondria and/or sarcoplasmic reticulum in some muscle fibres, groups of COX-negative fibres and subsarcolemmal increase of enzyme histochemical activity (Figure 2). Gömöri trichrome-stained cryostat sections showed moderately increased accumulation of subsarcolemmal fuchsinophilic material and minor lipid accumulation in a few muscle fibres by Oil Red O staining (Figure 2). There were no ragged-red fibres (Figure 2). In both patients, *MICU1* mutations resulted in loss of protein expression in skeletal muscle (Figure S2).

Electron microscopic investigation of quadriceps muscle biopsies of the 40-month-old patient 1 and of the 32-month-old patient 2 revealed severe mitochondrial pathology including enlarged mitochondria showing abnormal cristae and accumulation of electron-dense material (most likely corresponding to protein aggregates) within the mitochondrial matrix (Figure 3). In addition, inordinate glycogen

deposits at the I-bands of the sarcomere structures were found in patient 1 (Figure 3). Further pathomorphological findings included proliferated and de-organised ER-Golgi structures and the presence of vacuoles occasionally filled with glycogen deposits and/or other electron-dense material most likely corresponding to aggregated proteins (Figure 3). These vacuoles were frequently located adjacent to abnormally lobulated myonuclei (Figure 3).

CARS is a non-linear variant of Raman spectroscopy employed here to investigate the biochemical composition of muscle biopsies without any dyes, labels or prior assumptions. CARS microscopy performed on muscle biopsies derived from the two *MICU1* and two IBM patients as well as three adult and three juvenile controls (histological examination did not reveal any signs of myopathic features or neurogenic muscular atrophy) revealed increased signals for

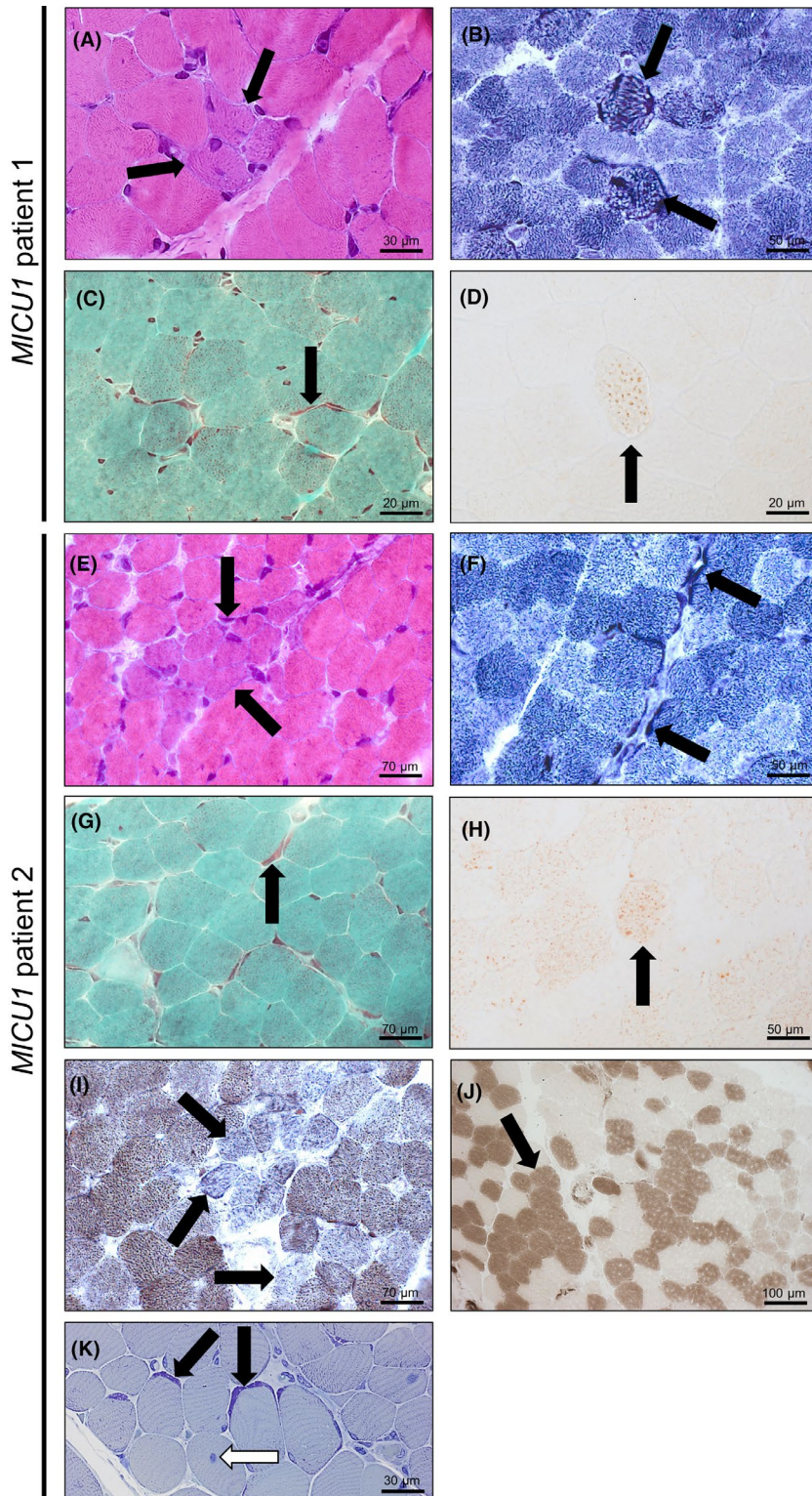


**FIGURE 2** Light microscopic findings in the *MICU1* patient-derived muscle biopsies. (A) Haematoxylin & eosin (H&E) staining of quadriceps muscle biopsy of index patient 1 reveals grouping of lesional basophilic muscle fibres (black arrows). (B) Focally increased NADH-labelling in a proportion of *MICU1*-diseased muscle fibres consistent with the accumulation of mitochondria and/or sarcoplasmic reticulum (black arrows). (C) Gömöri trichrome-stained cryostat sections showing moderate increased accumulation of subsarcolemmal fuchsinophilic material (black arrow). (D) Oil Red O-stained cryostat sections showing lipid accumulation in few muscle fibres (black arrow). (E) H&E staining of quadriceps muscle biopsy of index patient 2 reveals grouping of lesioned basophilic muscle fibres (black arrows). (F) Increased subsarcolemmal NADH-labelling in a proportion of muscle fibres (black arrows). (G) Gömöri trichrome-stained cryostat sections showing moderate increased accumulations of subsarcolemmal fuchsinophilic material (black arrow). (H) Oil Red O-stained cryostat sections showing lipid accumulation in few muscle fibres (black arrow). (I) COX-SDH staining revealed groups of COX-negative but SDH-positive (blue) fibres indicative for mitochondrial dysfunction (black arrows). (J) ATPase (pH: 4.2) staining revealed fibre-type grouping indicative for de-innervation processes (black arrows). (K) Toluidine blue staining of semi-thin sections shows calibre variations, subsarcolemmal increased staining corresponding to osmiophilic structures shown by EM (in Figure 3) and an internalised myonucleus (white arrow)



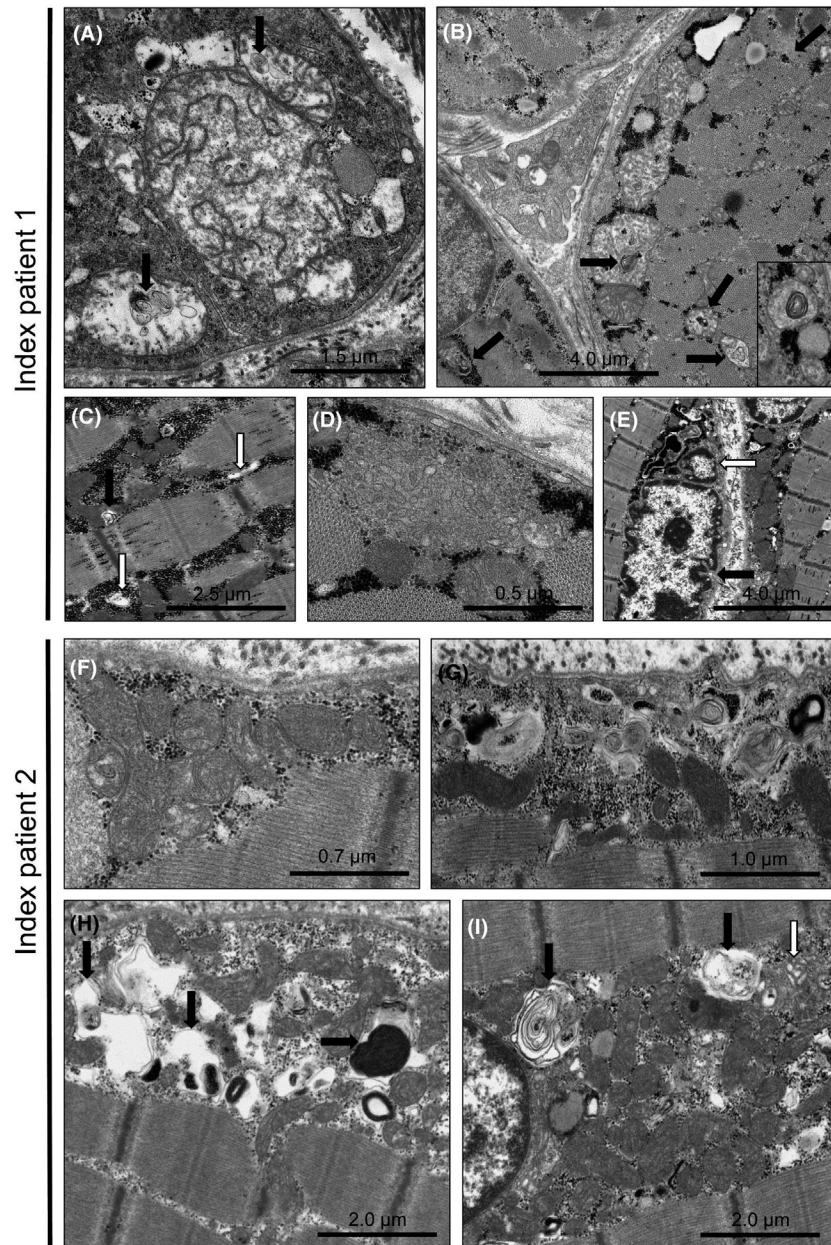


**FIGURE 3** Electron microscopic findings in the *MICU1* patient-derived muscle biopsies. A-E: patient 1 and F-I: patient 2. (A) Subsarcolemmal swollen mitochondrion with disintegrated cristae and deposits of myelin-like material in degenerating mitochondria (black arrows). (B) Degenerating mitochondria surrounded by glycogen deposits and occasionally filled with electron-dense material (black arrows) and vacuoles filled with glycogen. Insets show further mitochondria adjacent to glycogen accumulations with prominent inclusion of myelin-like material corresponding to aggregated protein. (C) Degenerating mitochondrion adjacent to glycogen accumulations with inclusions of myelin-like material (black arrow) and intramyofibrillar glycogen deposits as well as proliferated cisternae of the sarcoplasmic reticulum (white arrows). (D) Subsarcolemmal accumulation of vesicular structures presumably corresponding to disintegrated ER/SR-Golgi structures. (E) Abnormally lobulated (black arrow) and fragmented (white arrow) myonucleus with adjacent vacuoles prominently filled with electron-dense material. (F) Subsarcolemmally enlarged mitochondria showing abnormal cristae. (G) Subsarcolemmal accumulation of myelin-like, electron-dense material adjacent to normal and enlarged mitochondria. (H) Subsarcolemmal accumulation of proliferated ER/SR occasionally filled with myelin-like, electron-dense material (black arrows). (I) Accumulation of intermyofibrillar mitochondria adjacent to a non-subsarcolemmal myonucleus and associated with membranous structures in the cytoplasm suggestive of abnormal mitophagy (black arrows) and with proliferated vesicular structures presumably corresponding to Golgi vesicles (white arrow)

the wave numbers  $2930\text{ cm}^{-1}$ ,  $2885\text{ cm}^{-1}$  and  $2840\text{ cm}^{-1}$  in fibres of small calibre with particularly pronounced spot patterns in the *MICU1* patient samples (Figure 4). These cells commonly show an increased organisation of lipid structures at  $2885\text{ cm}^{-1}$  but not at

$2840\text{ cm}^{-1}$  (Figure 4). Given that mitochondria (in association with the SR/ER) are also involved in lipid synthesis [17], distribution patterns of lipids in *MICU1*-mutant muscle fibres were further examined. Applying unmixing, increases in abundance of spectra with

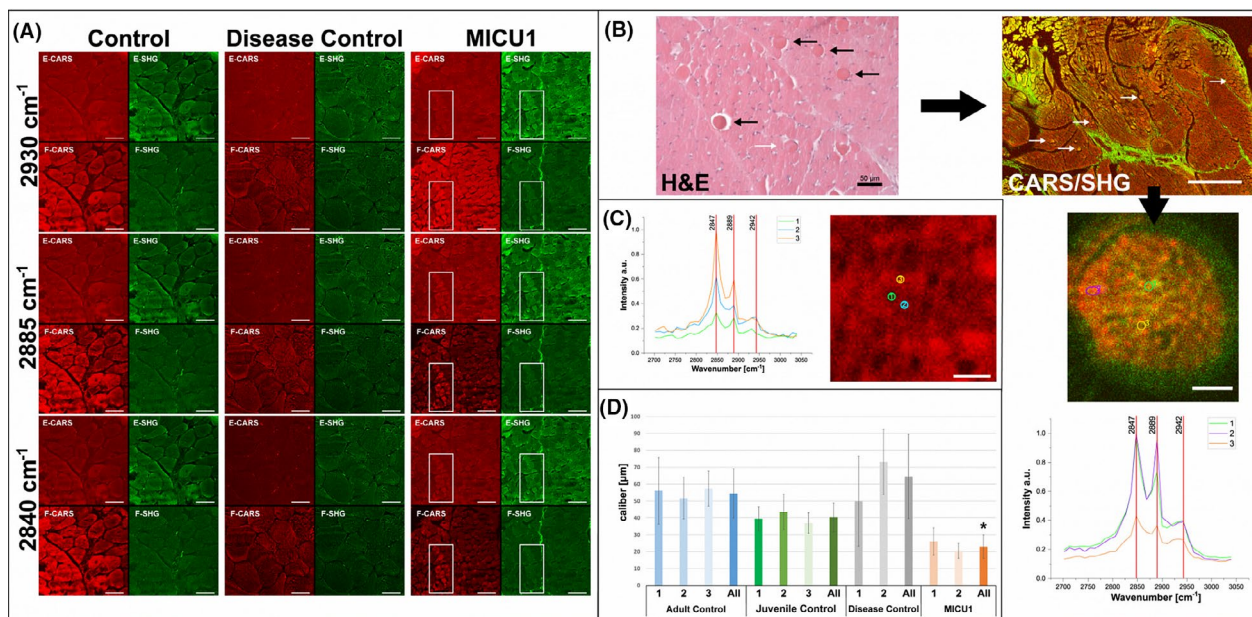


**FIGURE 4** CARS microscopic findings in the patient-derived muscle biopsies. (A) CARS and SHG contrast images of *MICU1* patient and control muscle biopsies. The *MICU1* patient-derived biopsies show clusters of muscle fibres with particularly pronounced spot patterns (white frames) not identified as such in the control and disease control muscles. Cells within these cluster present with increased protein ( $2930\text{ cm}^{-1}$  ( $\nu_s(\text{=CH}_3)$ ) and lipid ( $2889\text{ cm}^{-1}$  ( $\nu_{as}(\text{=CH}_2)$ ),  $2840\text{ cm}^{-1}$  ( $\nu_s(\text{=CH}_2)$ ), as well as SHG signals. Scale bars  $60\text{ }\mu\text{m}$ . (B) Round degenerating muscle fibres (black arrows) and fibres with reduced eosin staining (white arrow) were detected by H&E staining. In the superimposed CARS/SHG images (scale bar  $200\text{ }\mu\text{m}$ ), round muscle fibres of similar structure were also detectable, sometimes as groups or clusters (uppermost arrow). These cells have an internal granular structure (scale bar  $5\text{ }\mu\text{m}$ ) and granules have a higher intensity at  $2847\text{ cm}^{-1}$  than at  $2889\text{ cm}^{-1}$  indicating a lower lipid order (1). Besides, there are also elongated accumulations with a higher lipid order (2). Both structures show comparable protein signals at  $2930\text{ cm}^{-1}$ . Outside of these structures, the intensity of the three peaks is distinctively lower (3). The round muscle fibres are surrounded by SHG signals, maybe hinting to collagen or collagen-like structures. (C) Image of muscle fibre of a *MICU1* patient with autophagic vacuoles taken at  $2885\text{ cm}^{-1}$  (lipid spectra). Spectra are shown from different locations: low intensities of protein and lipids are measured within the vacuoles (1). Two typical spectra recorded around the vacuoles are also presented, which mostly differ in intensity (2, 3). Scale bar  $2.5\text{ }\mu\text{m}$ . (D) In the superimposed CARS/SHG images (scale bar  $200\text{ }\mu\text{m}$ ), round muscle fibres of similar structure were also detectable; sometimes as groups or clusters (uppermost arrow). These cells have an internal granular structure (scale bar  $5\text{ }\mu\text{m}$ ) and granules have a higher intensity at  $2847\text{ cm}^{-1}$  than at  $2889\text{ cm}^{-1}$  indicating a lower lipid order (1). Besides, there are also elongated accumulates with a higher lipid order (2). Both structures show comparable protein signals at  $2930\text{ cm}^{-1}$ . Outside of these structures, the intensity of the three peaks is distinctively lower (3). The round muscle fibres are surrounded by SHG signals, maybe hinting to collagen or collagen-like structures. (E) Comparison of the average muscle fibre calibers in the comparison of the controls with *MICU1* patients. Statistical details are given in supplemental document 1. Star: difference to all controls is of high statistical significance

high lipid but low protein content (represented through respective peaks) could be observed in muscle fibres of the two *MICU1* patients (Figure 4). In addition, sarcolemmal enrichment of lipids with focal clustering indicative for aggregate formation could be observed by unmixing in patient-derived muscle biopsy specimen compared to control samples (Figure 4, Figure S1).

The evaluation of the unmixing enables us to compare different parts of the fibre. Here, we compare the resulting spectra of the interior and the border of the fibre (Figure 4B, Figure S1). The spectra of the interior of control (endmember 1) and disease control (endmember 2) are quite similar in terms of peak position and ratio, and both are distinctively different from the one of *MICU1* patients (endmember 4). The spectra for the borders support this, but for control (endmember 3 + 4) and *MICU1* patients (endmember 2 + 5), there are now two spectra describing the border instead of just one. In contrast, there is just one for disease control (endmember 3). The

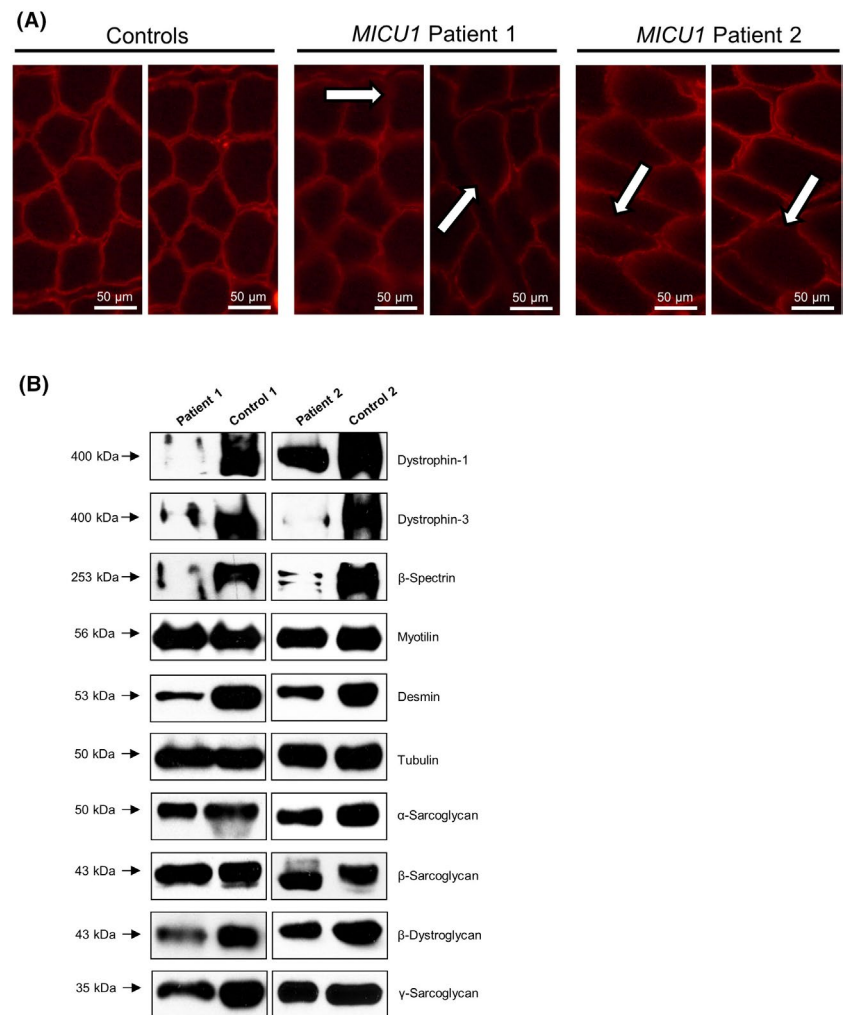
spectral comparison suggests a similarity of biochemical composition in control and disease control, while the composition of muscle fibres of *MICU1* patients is different, both inside the fibre and at its border.

Furthermore, CARS microscopy revealed the presence of areas with low signal intensity, sized between  $0.5$  and  $1.5\text{ }\mu\text{m}$  (Figure 4). Those areas, which most likely represent (autophagic) vacuoles, show considerably lower peaks for all three wave numbers mentioned above, thus suggesting that those are not densely packed with aggregates of lipids or proteins. However, the disease controls also present with vacuoles, but with diameters ranging from  $0.5$  to  $20\text{ }\mu\text{m}$ . Furthermore, rimmed vacuoles were found in one disease control and filled vacuoles in the two disease controls (black arrows in Figure S1).

Moreover, degenerating muscle fibres presented with granular appearance in CARS microscopy defined by a dominant peak



**FIGURE 5** Protein studies on *MICU1* patient-derived muscle biopsy specimen. (A) Immunofluorescence studies on cryopreserved muscle sections reveal reduced subsarcolemmal immunoreactivity of  $\beta$ -Spectrin (white arrows) in the quadriceps biopsy of both *MICU1* patients compared to control muscles. (B) Immunoblot studies on whole muscle protein extracts reveal reduced level of  $\beta$ -Spectrin, Dystrophin,  $\beta$ -Dystroglycan and Desmin while level of  $\alpha$ -,  $\beta$ - and  $\gamma$ -Sarcoglycan, Tubulin and Myotilin remain unchanged in the muscle of both patients compared to controls



a wave number  $2840\text{ cm}^{-1}$  suggesting that lipid organisation is lower than observed in the above mentioned small-calibre fibres (Figure 4B). In addition, degenerating fibres are characterised by a SHG-signal suggestive for the presence of structured protein aggregates, a hallmark of cell degeneration [18,19]. To quantify changes in muscle fibre calibres, the diameter of muscle cells were calculated resulting in an averaged fibre diameter of  $54.48\ \mu\text{m} \pm 14.67\ \mu\text{m}$  in adult controls,  $40.29\ \mu\text{m} \pm 8.54\ \mu\text{m}$  in juvenile controls,  $64.47\ \mu\text{m} \pm 24.94\ \mu\text{m}$  in disease controls and  $23.01\ \mu\text{m} \pm 6.83\ \mu\text{m}$  in *MICU1* patients (Figure 4) thus indicating muscle fibre atrophy in *MICU1* patients as previously described by Logan and co-workers [5]. However, quantification of muscle fibres per area ( $\text{mm}^2$ ) revealed an average of 289 fibres in controls and 1534 fibres in *MICU1* patients (data not shown; not performed for disease controls).

Immunofluorescence-based analysis of patient-derived biopsies revealed reduced subsarcolemmal immunoreactivity of  $\beta$ -Spectrin in approximately 20% of *MICU1*-mutant muscle fibres of both patients (Figure 5A). The decreased sarcolemmal distribution of  $\beta$ -Spectrin in muscle fibres of *MICU1* patients correlated with decreased protein abundance in whole muscle protein extracts analysed by immunoblot studies. Moreover, immunoblotting studies revealed decreased

abundances of further costameric proteins including Dystrophin,  $\beta$ -Dystroglycan and Desmin. In contrast,  $\alpha$ -,  $\beta$ - and  $\gamma$ -Sarcoglycan, Myotilin and Tubulin revealed normal results (Figure 5B).

### Lymphoblastoid patient cells lack *MICU1* and display dysregulation of mitochondrial $\text{Ca}^{2+}$ uptake

Lymphoblastoid cells derived from the homozygous patient 1 (red), healthy sibling (black) and heterozygous father (grey) were permeabilised in suspension and were used for fluorometric measurements of mitochondrial  $\text{Ca}^{2+}$  uptake (Figure 6A). Upon addition of a  $\text{Ca}^{2+}$  bolus that increased  $[\text{Ca}^{2+}]_c$  to  $\sim 1.5\ \mu\text{M}$ , only the homozygous patient cell mitochondria displayed  $\text{Ca}^{2+}$  clearance (left panel). By contrast, when  $[\text{Ca}^{2+}]_c$  was elevated above  $10\ \mu\text{M}$ , the homozygous patient cell mitochondria showed lesser  $\text{Ca}^{2+}$  uptake than mitochondria of either the healthy sibling or heterozygous father (middle panel). Quantitative analysis of the  $\text{Ca}^{2+}$  clearance rates obtained with various  $\text{Ca}^{2+}$  boluses, a dose-response plot was compiled that revealed suppressed  $\text{Ca}^{2+}$  dependence of the mitochondrial  $\text{Ca}^{2+}$  uptake in the patient cells (right panel). Mitochondrial  $\text{Ca}^{2+}$  uptake by the patient cells (patient 1)

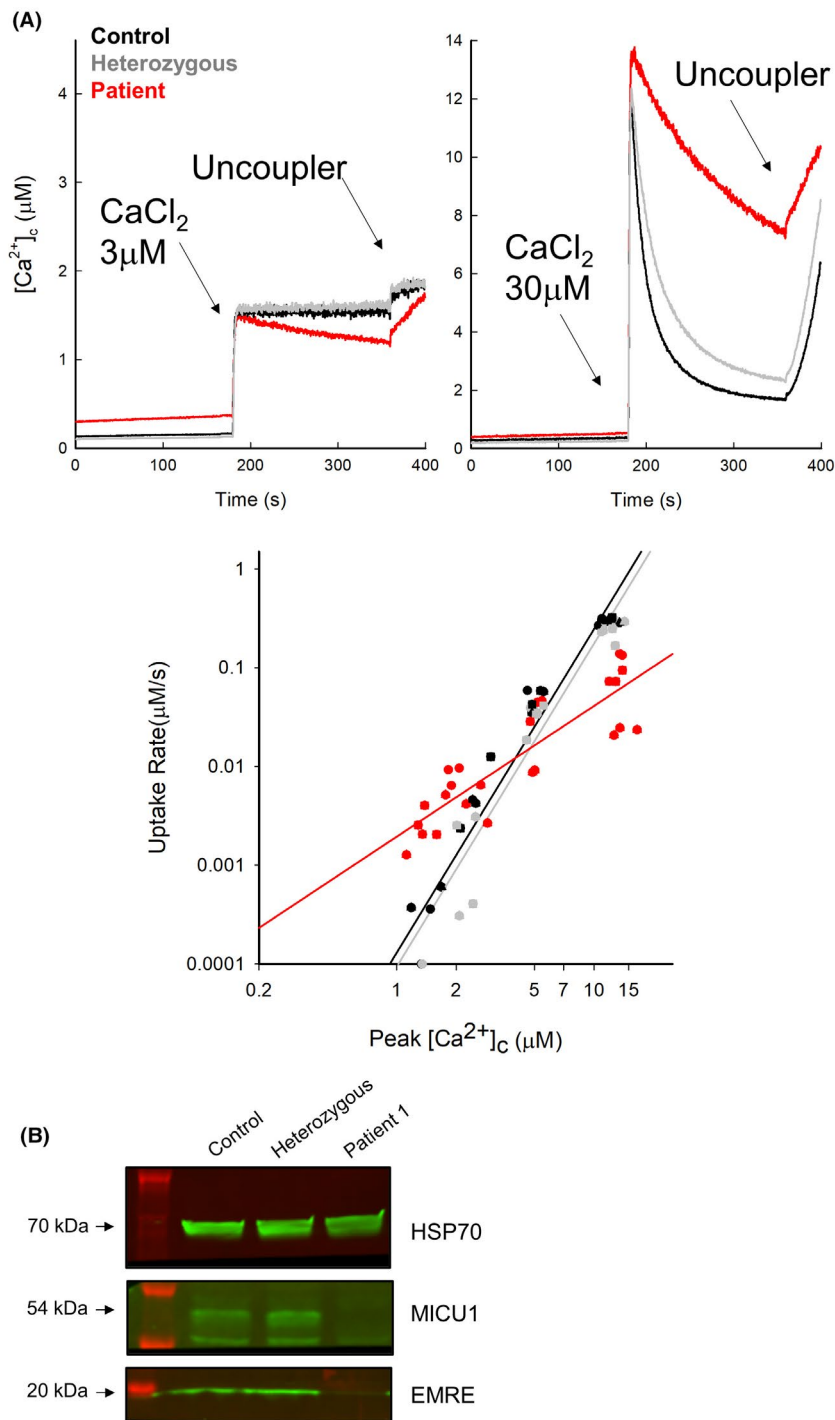


**FIGURE 6**  $\text{Ca}^{2+}$  dependence of mitochondrial  $\text{Ca}^{2+}$  uptake and MICU1 abundance in lymphoblastic cells of the patient and healthy and heterozygous family members. (A) Mean  $[\text{Ca}^{2+}]_c$  time courses measured using fura2FA (upper left panel) and fura2FFFA (upper right panel) in suspensions of permeabilised lymphoblastic cells show the mitochondrial clearance of a  $3 \mu\text{M}$  or  $30 \mu\text{M}$   $\text{CaCl}_2$  bolus (left and right panel respectively). Thapsigargin ( $2 \mu\text{M}$ ) and CGP-37157 ( $20 \mu\text{M}$ ) were included in the buffer to prevent endoplasmic reticulum  $\text{Ca}^{2+}$  uptake and mitochondrial  $\text{Ca}^{2+}$  extrusion respectively. Means were calculated for three independent experiments that included 2–3 measurements for each cell type. Lower panel:  $[\text{Ca}^{2+}]_c$  dose response of the initial mitochondrial uptake rates for different  $\text{Ca}^{2+}$  boluses recorded as shown in the upper left and right panels. The  $\text{CaCl}_2$  doses added were (in  $\mu\text{M}$ ) 3, 7, 15 and 30. Each symbol represent a measurement of one of the three separate experiments marked by circle, square and triangle symbols respectively. (B) Representative immunoblots showing the abundance of MICU1, EMRE and Heat Shock Protein 70 (HSP70) proteins from the cell suspension samples harvested in the end of the fluorometric measurements shown in A. HSP70 was used as a mitochondrial loading control. Images are representative for three different experiments

phenocopied the pattern previously observed with other MICU1-deficient cells [2,6]. Lysates prepared from the cells were used for immunoblotting that showed loss of the MICU1 band in the homozygous patient (Figure 6B). Notably, the MICU1 bands as well as the mitochondrial  $\text{Ca}^{2+}$  uptake phenotypes were similar in the healthy sibling (control) and the heterozygous father (Figure 6A). Immunoblot for EMRE that is required for the assembly of the MCU pore also showed a decrease in the homozygous patient, replicating a likely compensatory decrease in the uniporter abundance, which has been documented previously in cell lines [7,11,20] but

not in patients [9]. This result has indicated that loss of MICU1 can initiate changes in the abundance of other proteins which are not directly targeted by the genetic impairment.

### MICU1 mutations alter protein compositions in lymphoblastoid cells

Proteomic profiling utilising lymphoblastoid cells derived from patient 1 and the healthy sibling were carried out and allowed the

quantification of 2703 proteins, of which 800 presented with at least two unique peptides and a  $p$ -ANOVA  $<0.05$  (Figure 7A). The proteomic response to the novel *MICU1* mutation revealed increased abundance of 19, and decreased abundance of 20 proteins (Figure 7B,C). An overview of all affected proteins along with their subcellular localisations and functions is also provided in Figure 7. The proteomic signature of lymphoblastoid cells derived from our *MICU1* patient 1 revealed altered abundance of five proteins localising to mitochondria including interferon-induced protein with tetratricopeptide repeats 2 (IFIT2), caspase-1 (CASP1), protein-glutamine gamma-glutamyltransferase 2 (TGM2), succinate-semialdehyde dehydrogenase (SSDH) and bifunctional methylenetetrahydrofolate dehydrogenase/cyclohydrolase (MTDC) (Figure 7). Whereas five additional affected proteins (not

primarily localised to mitochondria) play known roles in the modulation of mitochondrial morphology and function. These proteins include Syntaxin-5 (STX5), Spectrins (SPTAN1 and SPTBN1), MTDC and Vimentin (VIM). Moreover, six affected proteins act in a  $Ca^{2+}$ -dependent manner or are involved in  $Ca^{2+}$  signalling pathways including calcium/calmodulin-dependent protein kinase type IV (CAMK4), vacuolar protein sorting-associated protein 37B (VPS37B), Drebrin (DBN1), Vimentin (VIM), Coactosin-like protein (COTL1), Endoplasmic (HSP90B1/ GRP94). The proteomic data have been deposited to the ProteomeXchange Consortium via the PRIDE [21] partner repository with the data set identifier PXD008867. Pathogenic mutations in genes corresponding to the affected proteins have been excluded by our sequencing data.

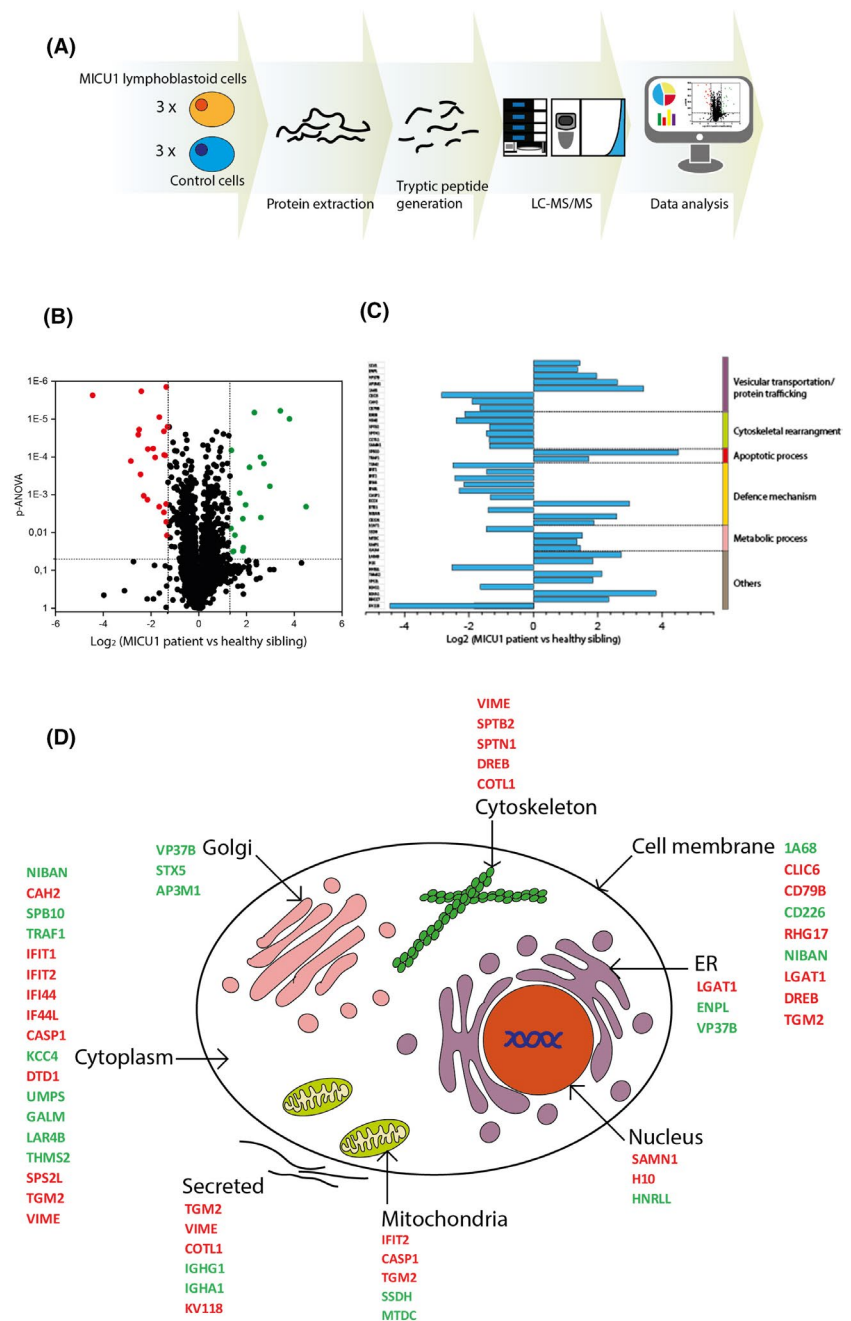


**FIGURE 7** Unbiased proteomic profiling of lymphoblastoid cells derived from *MICU1* patient 1. (A) Applied proteomic workflow. (B) Volcano plot of obtained proteomic results (red dots represent proteins decreased and green dots proteins increased in abundance). (C) Categorisation of proteomic findings according to the function of the proteins affected in abundance upon the presence of the homozygous p.(Arg185\*) mutation. (D) Subcellular localisations of the proteins affected in abundance upon the presence of the homozygous p.(Arg185\*) mutation (red-labelled proteins are decreased and green-labelled proteins are increased in abundance)



## Immunostaining studies allow recapitulation of proteomic findings and provide further evidence for associated pathophysiologies in MICU1 patient-derived muscle

Proteomic profiling on lymphoblastoid cells revealed the altered abundance of 39 proteins (see above). To further confirm this finding and demonstrate a similar pathobiochemical impact of MICU1 loss in muscle cells, immunostaining studies were carried out for paradigmatic proteins. These studies confirmed an increase of Syntaxin-5 (STX5) and Endoplasmic reticulum chaperone (GRP94), two proteins localising to the ER–Golgi network, also in muscle cells. To further study the potential proliferation of ER–Golgi structures indicated by the results of our ultrastructural investigation, immunostaining for POC1A, a protein resident to this functional continuum, was performed showing an increased immunoreactivity in a proportion of MICU1-mutant muscle cells (Figure S2). Based on this finding, we additionally studied the level of Calreticulin (CALR) and BiP, two Ca<sup>2+</sup>-binding chaperones promoting protein quality control in the ER, along with Seipin (BSCL2), a protein mediating the formation and/or stabilisation of ER-lipid droplets and microtubule-associated proteins 1A/1B light chain 3B (LC-3) as well as lysosome-associated membrane glycoprotein 1 (LAMP1), two known protein aggregation markers. Compared to control muscle cells, focal increase was detected for these proteins in MICU1-mutant muscle cells (Figure S2). Given that caspase-1 (CASP1), acting as promoter of apoptosis in concert with cytochrome C (CytC), was identified with increased abundance in MICU1 patient-derived lymphoblastoid cells, CASP1 and CytC level were studied in patient-derived muscle. Both proteins showed a focal increase in muscle cells of MICU1 patients compared to controls cells (Figure S2). Prompted by the results of our immunoblotting studies suggesting a dysregulation of proteins involved in anchoring of the actin cytoskeleton to subcellular structures, additional immunostaining studies were carried out for Actinin-3 (ACTN3) and Integrin beta-4 (ITGB4): both proteins showed an irregular sarcoplasmic increase in MICU1 patient-derived muscles (Figure S2).

## DISCUSSION

### MICU1 deficiency-associated phenotypes

Loss-of-function point mutations have been identified in MICU1 as the cause of a rare neuromuscular and neurodevelopmental disease in children [13]. So far, the clinical spectrum of MICU1 patients included progressive proximal muscular dystrophy, elevated CK levels, generalised muscle weakness, positive Gower's manoeuvre, mild intellectual disability or learning difficulties and variable features such as episodic ataxia, skin involvement, ptosis, hypometropia, pendular nystagmus, bilateral optic atrophy, microcephaly and peripheral axonal neuropathy as well as elevated transaminase enzymes [5,9,16]. In addition, two cousins with a homozygous deletion involving exon 1 (chr 10: 74,385,085–74,387,860, size: 2,775 nucleotide pairs) of

MICU1 were described: one case presented with fatigue and lethargy associated with mild hypotonia, and global muscle weakness among other symptoms such as episodes of accompanied viral infections but normal psychomotor development. Remarkably, the other case carrying the same homozygous deletion presented with a more pronounced phenotype characterised by additional migraines, pendular nystagmus, cataracts and mild learning difficulties [22]. Muscle biopsy studies commonly revealed rare atrophic fibres and increased internal nuclei. The variable clinical presentation resulting from MICU1 deficiency in this family underlines the broad clinical spectrum of the disease and shows that a clear genotype–phenotype correlation did not emerge. Further 'larger' genetic rearrangements associated with the clinical manifestation of a MICU1 phenotype include a heterozygous intragenic duplication of exons 9 and 10 [16] and a homozygous deletion of exon 1 [22].

Here, we describe two new MICU1 patients, one carrying the recently described homozygous Middle Eastern founder mutation (chr10: 74268012 G > A; c.553C>T; p.(Arg185\*); minor allele frequency of 1:60,000 in the ExAC database, but in ~1:500 individual in the Middle East [16]) and the other compound heterozygous nonsense p.(Arg18\*) mutation combined with an intragenic deletion affecting exon 2 (the two latter mutations have not been observed previously). Both patients presented with developmental delay, highly elevated CK level, and histological and ultrastructural changes in muscle biopsy specimens compatible with a myopathy associated with MICU1 deficiency. Moreover, the phenotype of both patients was dominated by the presence of ataxia suggesting that this clinical feature is one of the symptoms more frequently present in this multisystemic disease. Notably, further clinical findings in our patients included clinodactyly, hyperactivity and insomnia as well as impaired cognitive pain perception (due to restlessness and attention problems) thus expanding the currently known phenotypic spectrum of MICU1 deficiency.

### Microscopic biopsy findings in muscle biopsy specimen of MICU1 patients in correlation with proteomic signature of lymphoblastoid cells

Microscopic studies of the muscle biopsies, including light, electron and CARS microscopic examinations, revealed the loss of MICU1 expression based on the respective molecular genetic defects leading to atrophy affecting slow and fast muscle fibres. According to the subcellular localisation and function of MICU1, severe mitochondrial perturbations in the muscle fibres were indicated by histological findings and moreover clearly identified by electron microscopy. This observation accords with the previously described mitochondrial fragmentation in fibroblasts upon deficiency of functional MICU1 and perturbed Ca<sup>2+</sup> homeostasis [9] as also exemplified in our in vitro model (Figure 6). Further ultrastructural changes include disintegration of ER–Golgi structures and the presence of vacuoles filled with protein aggregates expanding the currently known spectrum of ultrastructural abnormalities associated with MICU1 deficiency.

Proteomic profiling results obtained from lymphoblastoid cells presented in this study revealed altered abundances of proteins belonging to the functional ER–Golgi network. Interestingly, impaired function of this network (also mirrored in disintegrated morphology) has been often linked to impaired protein processing and build-up of (autophagic) vacuoles in a variety of neurological diseases.

CARS microscopy can provide spatially resolved information about the biochemical composition of the sample, and by such, also resolve morphological structures or respective alterations. Here, our CARS microscopic studies revealed an increased organisation of lipid structures in a proportion of small-calibre muscle fibres in both *MICU1* patients. Given that lipids are synthesised at distinct parts of the cell including the ER–Golgi network and mitochondria [23], and these organelles in turn form a functional continuum due to the formation of mitochondria-associated ER membranes (MAMs), also involved in the transport of  $Ca^{2+}$  [24–26] and based on lipid synthesis [17], an influence of *MICU1* deficiency on proper cellular lipid homeostasis can be hypothesised. In this context, immunoblot studies of Seipin (BSCL2), a protein mediating the formation and/or stabilisation of endoplasmic reticulum-lipid droplets, revealed increased abundance in *MICU1* patient-derived muscles (Figure S2). In addition, the absence of a respective lipid peak in degenerating muscle fibres suggests that the increased appearance of organised lipid structures does not represent a pathophysiological correlate of initiated apoptosis. In contrast, muscle cells were characterised by the presence of protein accumulations identified by CARS microscopy. Given that lipids are the building blocks of cellular membranes such as the muscle cell plasma membrane, the CK-increase observed in *MICU1* patients might also be caused by increased membrane permeability as an effect of impaired lipid homeostasis. However, additional lipidomic investigations in combination with functional studies of membrane permeability on (cultured) *MICU1*-deficient muscle cells would be needed to confirm this assumption. In addition, our CARS microscopic findings confirmed the presence of vacuoles in *MICU1*-deficient muscle fibres. However, the considerable reduced peaks of the three measured wave numbers suggested that neither lipids nor proteins are enriched within these vacuoles appearing as areas with low signal intensity in the contrast representation of the CARS measurements. Electron microscopic studies (see above) revealed the presence of small vacuoles which are only occasionally filled with myelin-like (electron-dense) material most likely corresponding to protein and/or lipid aggregates.

### Mitochondrial and cytoskeletal pathology caused by deficiency of functional *MICU1*

The dysregulation of 16 proteins (40% of all vulnerable proteins) can be directly linked to altered mitochondrial  $Ca^{2+}$  handling and thus *MICU1* dysfunction resulting in ultrastructural mitochondrial pathology (swollen mitochondria, cristae-disorganisation and build-up of aggregates within the mitochondrial matrix; Figure 3). This biochemical finding accords with the proven perturbed  $Ca^{2+}$  homeostasis

in the patient-derived lymphoblastoid cells (Figure 6) and provides novel insights into the biochemical consequences. Importantly, perturbed  $Ca^{2+}$  homeostasis has already been described in fibroblasts derived from *MICU1* patients.[9]

A growing body of evidence suggests that mitochondrial morphology and function are modulated by the cytoskeleton via mostly uncharacterised pathways [27] and our proteomic findings hint towards a vulnerability of cytoskeleton upon loss of *MICU1* by altered abundance of SPTBN1, SPTAN1, DBN1, VIM and COTL1. Vulnerability of Spectrin could also be observed by immunological investigations in the muscle biopsies of our two *MICU1* patients (Figure 5). Interestingly,  $Ca^{2+}$  is known to modulate the stabilisation of Actin–Spectrin complexes [28] and altered mitochondria with impaired capacity to buffer receptor-gated  $Ca^{2+}$  fluxes have already been linked to promotion of  $Ca^{2+}$ -activated proteases and subsequent degradation of the Spectrin meshwork [29], thus confirming a tight connection between mitochondrial and Spectrin homeostasis. In addition, DBN1, VIM and COTL1 are also proteins that bind to actin in a  $Ca^{2+}$ -dependent manner [30–32], which functioning in concert with Spectrins, modulate actin dynamics. Of note, immunoblotting studies on patient-derived muscle protein extracts revealed decreased abundance of further costameric proteins including Dystrophin,  $\beta$ -Dystroglycan and Desmin supporting the concept of a perturbed anchoring of the actin cytoskeleton to the sarcolemma as part of *MICU1*-associated pathophysiology. In addition, perturbed anchoring of the Actin cytoskeleton to organelles and/or the sarcolemma is suggested by the irregular sarcoplasmic increase of ITGB4 and ACTN3, two proteins involved in anchoring of Actin to a variety of intracellular structures, in *MICU1* patients (Figure S2). However, additional functional and structural studies on single isolated fibres would be needed to elucidate this pathobiochemical interplay more precisely. Given that impairment of cytoskeletal dynamics and mitochondrial dysfunction are commonly observed in many neurodegenerative and neuromuscular disorders [1,33–37], it seems to be plausible that vulnerability of regular cytoskeletal composition results from *MICU1* deficiency-based mitochondrial dysfunction and significantly contributes to the phenotypical manifestation of loss-of-function *MICU1* mutations in different tissues. Remarkably,  $\beta$ -III-Spectrin spinocerebellar ataxia type 5 mutation reveals a dominant cytoskeletal mechanism that underlies dendritic arborisation [38].

### ER–Golgi pathology and the presence of autophagic vacuoles caused by loss of functional *MICU1*

Altered abundance of ER–Golgi proteins might accord with mitochondrial vulnerability and could represent a secondary pathophysiological mechanism: proteomic profiling revealed increased Syntaxin-5 (SNX5), which belongs to the SNARE complex facilitating the transport of cholesterol to mitochondria [39] (lipid accumulation has been identified in *MICU1* patients based on our CARS microscopic studies), and SNX5 is also involved in vesicle tethering and fusion at the cis-Golgi membrane to maintain the stacked and inter-connected structure of the Golgi apparatus. Interestingly, our immunological

studies on muscle biopsy specimen confirmed an increase of SNX5, as well as an increase of POC1A, an ER–Golgi-resident protein, in a proportion of *MICU1*-mutant muscle cells (Figure S2). In addition, electron microscopy showed a build-up of proliferated and de-organised ER–Golgi structures (Figure 3). A potential impact of altered Golgi architecture—as observed in the muscle biopsies—on regular vesicular transport can also be deduced from our proteomic findings through the altered abundance of vesicular trafficking regulators such as VPS37B and AP-3 complex subunit mu-1 (AP3 M1): VPS37B is a  $\text{Ca}^{2+}$ -dependent binding protein of the endosomal sorting complexes required for transport (ESCRT) required for vesicular trafficking processes [40]. AP3 M1 is part of the AP-3 adaptor complex, which associates with the Golgi, facilitates the budding from the Golgi and may be directly involved in trafficking to the endosomal or lysosomal system [41]. The expression of the AP-3 complex is essential for the biogenesis of acidic  $\text{Ca}^{2+}$  and polyphosphate organelles (so called acidocalcisomes) including lysosomes [42] with various functions including autophagy [43]. Interestingly, the results of our ultrastructural investigations revealed the presence of autophagic vacuoles (occasionally filled with electron-dense material) in muscle fibres of our patients (Figure 3). Thus, one might speculate that increased expression of AP3 M1 and other proteins involved in proteolysis such as Serpin B10 (SBP10; increased in the patient-derived lymphoblastoid cells) accords with the presence of vacuoles in the muscle biopsies of *MICU1* patients. This assumption is supported by the results of our immunostaining studies on patient-derived muscle biopsies showing an increase of LAMP1 and LC-3, two protein aggregation markers involved in modulation of autophagy (Figure S2). Along this line, data of our proteomic profiling on lymphoblastoid cells revealed increased abundance of FAM129A (protein Niban). Niban has recently been linked to autophagy-induction activated by perturbed  $\text{Ca}^{2+}$  homeostasis and ER stress [44]. Potential consequences of *MICU1* mutations on the intracellular  $\text{Ca}^{2+}$  dynamics in ER–mitochondria crosstalk [45] are further supported by the identified increased abundance of Endoplasmic reticulum chaperone of the ER [46], in both *MICU1* patient-derived lymphoblastoid cells and muscle. Also, the increase of BiP and Calreticulin in patient-derived muscle cells accords with this concept.

### Activation of pro-apoptotic and pro-survival mechanisms caused by *MICU1* mutation

Apart from a role of AP-3 in Golgi maintenance and protein clearance, a correlation between AP-3-function and the interferon signalling pathway has been described [47], and dysregulation of interferon proteins (along with caspases and B-cell lymphoma-protein 2 (BCL2); Tab. 1) as observed in our proteomic data is known to lead to cellular apoptosis by inducing the expression of several apoptotic regulators (including caspases and BCL2) via a mitochondrial pathway [48]. Along this line, increased abundance of SBP10 and TNF receptor-associated factor 1 (TRAF1) accords with potential induction of apoptosis [49,50]. In this context, it is important to note that a

recent study demonstrated the control of TRAF1 along with CAMK4 (also increased in our *in vitro* system) on the molecular genetic level upon muscle loading highlighting their involvement in muscle fibre hypertrophy and thus muscle cell survival [51]. Induction of apoptotic processes in *MICU1* patient-derived muscle cells is indicated by the combined increase of CASP1 and CytC (Figure S2), in turn supporting the relevance of proteomic findings obtained in the lymphoblastoid cells. However, an increased abundance of proteins with neuroprotective properties have also been identified, in agreement with the concept of activation of pro-survival mechanisms: Uridine 5'-monophosphate synthase (UMPS) is involved in synthesising UMP from orotate and deficiency of UMPS has been linked to hereditary orotic aciduria, which is associated with some degree of physical and mental retardation [52]. Succinate-semialdehyde dehydrogenase (ALDH5A1) catalyses one step in the degradation of the inhibitory neurotransmitter gamma-aminobutyric acid [53]. Additionally, MTHFD2 (human MTDC), also elevated in the lymphoblastoid cells of our patient, modulates neuronal development via mitochondrial formate production [54,55] and thus most likely antagonises mitochondrial vulnerability in tissue upon loss of functional *MICU1*.

### Biochemical and clinical synopsis

We hypothesise that impaired  $\text{Ca}^{2+}$  dynamics and concomitant increase in lipid clustering, as well as dysregulation of proteins involved in metabolic processes (Figure 7) do reversibly and transiently affect cellular metabolic processes (also influencing further cellular function such as protein trafficking). This might accord with the observation of fluctuating symptoms in *MICU1* patients such as episodes of pain-related unsteady gait in patient 1 as well as transient infection-induced ataxia and exercise-related episodic pain in patient 2.

In summary, we describe novel, loss-of-function mutations of *MICU1* in two patients expanding the mutational and clinical spectrum of the disease. Our combined ultramorphological, functional, proteomic and microscopic studies of human samples provide new insights into the molecular aetiology of the disease and point out that perturbed  $\text{Ca}^{2+}$  homeostasis caused by loss of functional *MICU1* might affect cellular functions and organelle compositions beyond mitochondrial maintenance including lipid homeostasis, vulnerability of cytoskeletal components such as Spectrin as well as of the ER–Golgi network impacting on proper protein clearance. However, biochemical studies on cells and/or muscle biopsies of further *MICU1* patients confirming the data described here are needed to finally declare our findings as pathophysiological cascades resulting from the loss of functional *MICU1*.

### ETHICS APPROVAL:

The ethics committee of University Medicine Essen (19-9011-BO) had granted ethical approval. The legal guardians of the patients gave consent for the performed analyses.



## ACKNOWLEDGEMENTS

This study was supported by the 'Ministerium für Kultur und Wissenschaft des Landes Nordrhein-Westfalen', the 'Regierenden Bürgermeister von Berlin - Senatskanzlei Wissenschaft und Forschung' and the 'Bundesministerium für Bildung und Forschung', also in form of the Leibniz-Research-Cluster (grant number: O31A360E). This work was also supported by a grant of the French Muscular Dystrophy Association (AFM-Téléthon) (#21466) to AR and by an NIH grant (RO1 GM102724) to GH. The research leading to these results has also received funding from the European Community's Seventh Framework Programme (FP7/2007-2013) under grant agreement n° 2012-305121 'Integrated European - omics research project for diagnosis and therapy in rare neuromuscular and neurodegenerative diseases (NEUROMICS)'. RH is a Wellcome Investigator (109915/Z/15/Z), who receives support from the Medical Research Council (UK) (MR/N025431/1), the European Research Council (309548) and the Newton Fund (MR/N027302/1). HL receives support from the Canadian Institutes of Health Research (Foundation Grant FDN-167281), the Canadian Institutes of Health Research and Muscular Dystrophy Canada (Network Catalyst Grant for NMD4C), the Canada Foundation for Innovation (CFI-JELF 38412) and the Canada Research Chairs program (Canada Research Chair in Neuromuscular Genomics and Health, 950-232279). The authors also acknowledge support from deCODE genetics. Parts of this study were financed in the framework of the NME-GPS project by the European Regional Development Fund (ERDF). The authors thank Mrs. Hannelore Mader, Mrs. Claudia Krude, Mrs. Eveline Pascual, Mrs. Swantje Hertel, Mrs. Nancy Meyer and Mr. Fabian Förster for their expert technical assistance.

## CONFLICT OF INTEREST

The authors declare no conflict of interest.

## AUTHOR CONTRIBUTIONS

NK, ME, EF, RH, AR and JW designed the study. Clinical examinations of the patients have been carried out by MH, ME, SZ and NK. Genetic analyses were performed by AT, KE, TE and CG. Lymphoblastoid cells were generated by TE, KE and NK. Light- and electron microscopic as well as immunoblot studies were performed by JW. Immunofluorescence and proteomic studies were performed by AR and VP. CARS microscopic studies were carried out by AC and EF. Ca<sup>2+</sup> transport studies were carried out by GH, KTH and AB. The manuscript was drafted by AR, MH, AC, GH, HL, RH and JW, and proofread as well as approved by all the authors.

## PEER REVIEW

The peer review history for this article is available at <https://publons.com/publon/10.1111/nan.12694>.

## DATA AVAILABILITY STATEMENT

The proteomic data have been deposited to the ProteomeXchange Consortium via the PRIDE partner repository with the data set identifier PXD008867.

## ORCID

Adam Bartok  <https://orcid.org/0000-0002-1232-5246>

Erik Freier  <https://orcid.org/0000-0002-0559-4210>

Andreas Roos  <https://orcid.org/0000-0003-2833-0928>

## REFERENCES

- Johri A, Beal MF. Mitochondrial dysfunction in neurodegenerative diseases. *J Pharmacol Exp Ther*. 2012;342(3):619.
- Csordás G, Golenár T, Seifert EL, et al. MICU1 controls both the threshold and cooperative activation of the mitochondrial Ca<sup>2+</sup> uniporter. *Cell Metab*. 2013;17(6):976-987.
- Mallilankaraman K, Doonan P, Cárdenas C, et al. MICU1 is an essential gatekeeper for MCU-mediated mitochondrial Ca<sup>2+</sup> uptake that regulates cell survival. *Cell*. 2012;151(3):630-644.
- Perocchi F, Gohil VM, Girgis HS, et al. MICU1 encodes a mitochondrial EF hand protein required for Ca<sup>2+</sup> uptake. *Nat*. 2010;467(7313):291-296.
- Logan CV, Szabadkai G, Sharpe JA, et al. Loss-of-function mutations in MICU1 cause a brain and muscle disorder linked to primary alterations in mitochondrial calcium signaling. *Nat Genet*. 2014;46:188.
- Antony AN, Paillard M, Moffat C, et al. MICU1 regulation of mitochondrial Ca<sup>2+</sup> uptake dictates survival and tissue regeneration. *Nat Commun*. 2016;7(1):10955.
- Liu JC, Liu J, Holmström KM, et al. MICU1 serves as a molecular gatekeeper to prevent in vivo mitochondrial calcium overload. *Cell Rep*. 2016;16(6):1561-1573.
- Frank S, Gaume B, Bergmann-Leitner ES, et al. The role of dynamin-related protein 1, a mediator of mitochondrial fission, in apoptosis. *Dev Cell*. 2001;1(4):515-525.
- Bhosale G, Sharpe JA, Koh A, Kouli A, Szabadkai G, Duchon MR. Pathological consequences of MICU1 mutations on mitochondrial calcium signalling and bioenergetics. *Biochim Biophys Acta Mol Cell Res*. 2017;1864(6):1009-1017.
- Kollipara L, Buchkremer S, Coraspe JAG, et al. In-depth phenotyping of lymphoblastoid cells suggests selective cellular vulnerability in Marinesco-Sjögren syndrome. *Oncotarget*. 2017;8(40):68493-68516.
- Paillard M, Csordás G, Huang K-T, Várnai P, Joseph SK, Hajnóczky G. MICU1 interacts with the D-ring of the MCU pore to control its Ca<sup>2+</sup> flux and sensitivity to Ru360. *Mol Cell*. 2018;72(4):778-85.e3.
- Kölbl H, HATHAZI D, ROOS A, SCHARA U. Identification of protein markers in skeletal muscle of laminin-211-deficient CMD type 1A-patients. *Front Neurol*. 2019;10:470.
- Xu X. MICU1 mutation: a genetic cause for a type of neuromuscular disease in children. *Clin Genet*. 2015;87(4):327-328.
- Ebersbach P, Stehle F, Kayser O, Freier E. Chemical fingerprinting of single glandular trichomes of *Cannabis sativa* by Coherent anti-Stokes Raman scattering (CARS) microscopy. *BMC Plant Biol*. 2018;18(1):275.
- Brauers E, Roos A, Kollipara L, et al. The Caveolin-3 G56S sequence variant of unknown significance: Muscle biopsy findings and functional cell biological analysis. *Proteomics Clin Appl*. 2017;11(1-2):1600007.
- Musa S, Eyaid W, Kamer K, et al. A Middle Eastern founder mutation expands the genotypic and phenotypic spectrum of mitochondrial MICU1 deficiency: a report of 13 patients (43, 79-83). Springer: JIMD Reports; 2018.
- Osman C, Voelker DR, Langer T. Making heads or tails of phospholipids in mitochondria. *J Cell Biol*. 2011;192(1):7.
- Crabbs TA. Skeletal muscle - Degeneration 2015 [updated 2015/03/11; cited 2019/ 02/11]. [https://ntp.niehs.nih.gov/nl/musculoskeletal/skel\\_musc/degen/index.htm](https://ntp.niehs.nih.gov/nl/musculoskeletal/skel_musc/degen/index.htm)
- Greaves P, Chouinard L, Ernst H, et al. Proliferative and non-proliferative lesions of the rat and mouse soft tissue, skeletal muscle and mesothelium. *J Toxicol Pathol*. 2013;26(3\_Suppl):15-26S.

20. Phillips CB, Tsai C-W, Tsai M-F. The conserved aspartate ring of MCU mediates MICU1 binding and regulation in the mitochondrial calcium uniporter complex. *Elife* [Internet]. 2019;01//; 8. <https://doi.org/10.7554/eLife.41112>
21. Vizcaino JA, Côté RG, Csordas A, et al. The Proteomics Identifications (PRIDE) database and associated tools: status in 2013. *Nucleic Acids Res*. 2012;41(D1):D1063-D1069.
22. Lewis-Smith D, Kamer KJ, Griffin H, et al. Homozygous deletion in MICU1 presenting with fatigue and lethargy in childhood. *Neurol Genet*. 2016;2(2):e59.
23. Scharwey M, Tatsuta T, Langer T. Mitochondrial lipid transport at a glance. *J Cell Sci*. 2013;126(23):5317.
24. Csordás G, Weaver D, Hajnóczky G. Endoplasmic reticulum-mitochondrial contactology: structure and signaling functions. *Trends Cell Biol*. 2018;28(7):523-540.
25. Lahiri S, Toulmay A, Prinz WA. Membrane contact sites, gateways for lipid homeostasis. *Curr Opin Cell Biol*. 2015;33:82-87.
26. Morciano G, Marchi S, Morganti C, et al. Role of mitochondria-associated ER membranes in calcium regulation in cancer-specific settings. *Neoplasia*. 2018;20(5):510-523.
27. Anesti V, Scorrano L. The relationship between mitochondrial shape and function and the cytoskeleton. *Biochim Biophys Acta Bioenerg*. 2006;1757(5):692-699.
28. Matsuoka Y, Li X, Bennett V. Adducin is an in vivo substrate for protein kinase C: phosphorylation in the MARCKS-related domain inhibits activity in promoting spectrin-actin complexes and occurs in many cells, including dendritic spines of neurons. *J Cell Biol*. 1998;142(2):485.
29. Seubert P, Peterson C, Vanderklish P, Cotman C, Lynch G. Increased spectrin proteolysis in the brindled mouse brain. *Neurosci Lett*. 1990;108(3):303-308.
30. Hofmann I, Herrmann H, Franke WW. Assembly and structure of calcium-induced thick vimentin filaments. *Eur J Cell Biol*. 1991;56(2):328-341.
31. Mercer JC, Qi Q, Mottram LF, et al. Chemico-genetic identification of drebrin as a regulator of calcium responses. *Int J Biochem Cell Biol*. 2010;42(2):337-345.
32. Provost P, Doucet J, Hammarberg T, Gerisch G, Samuelsson B, Rådmark O. 5-Lipoxygenase interacts with coactosin-like protein. *J Biol Chem*. 2001;276(19):16520-16527.
33. Cairns NJ, Lee VMY, Trojanowski JQ. The cytoskeleton in neurodegenerative diseases. *J Pathol*. 2004;204(4):438-449.
34. Dobbins GC, Zhang B, Xiong WC, Mei L. The role of the cytoskeleton in neuromuscular junction formation. *J Mol Neurosci*. 2006;30(1):115-117.
35. Jiang Z, Wang W, Perry G, Zhu X, Wang X. Mitochondrial dynamic abnormalities in amyotrophic lateral sclerosis. *Transl Neurodegener*. 2015;4(1):14.
36. Katsetos CD, Koutzaki S, Melvin JJ. Mitochondrial dysfunction in neuromuscular disorders. *Semin Pediatr Neurol*. 2013;20(3):202-215.
37. Ordóñez DG, Lee MK, Feany MB.  $\alpha$ -synuclein induces mitochondrial dysfunction through spectrin and the actin cytoskeleton. *Neuron*. 2018;97(1):108-24.e6.
38. Avery AW, Thomas DD, Hays TS.  $\beta$ -III-spectrin spinocerebellar ataxia type 5 mutation reveals a dominant cytoskeletal mechanism that underlies dendritic arborization. *Proc Natl Acad Sci USA*. 2017;114(44):E9376-E9385.
39. Fuller HR, Gillingwater TH, Wishart TM. Commonality amid diversity: Multi-study proteomic identification of conserved disease mechanisms in spinal muscular atrophy. *Neuromuscular disorders: NMD*. 2016;26(9):560-569.
40. Spallek T, Beck M, Khaled SB, et al. ESCRT-I mediates FLS2 endosomal sorting and plant immunity. *PLoS Genet*. 2013;9(12):e1004035.
41. Cowles CR, Odorizzi G, Payne GS, Emr SD. The AP-3 adaptor complex is essential for cargo-selective transport to the yeast vacuole. *Cell*. 1997;91(1):109-118.
42. Huang G, Fang J, Sant'Anna C, et al. Adaptor protein-3 (AP-3) complex mediates the biogenesis of acidocalcisomes and is essential for growth and virulence of *Trypanosoma brucei*. *J Biol Chem*. 2011;286(42):36619-36630.
43. Docampo R, Huang G. Acidocalcisomes of eukaryotes. *Curr Opin Cell Biol*. 2016;41:66-72.
44. Qaisiya M, Mardešić P, Pastore B, Tiribelli C, Bellarosa C. The activation of autophagy protects neurons and astrocytes against bilirubin-induced cytotoxicity. *Neurosci Lett*. 2017;661:96-103.
45. Patergnani S, Suski JM, Agnoletto C, et al. Calcium signaling around Mitochondria Associated Membranes (MAMs). *Cell Commun Signal*. 2011;9(1):19.
46. Marzec M, Eletto D, Argon Y. GRP94: An HSP90-like protein specialized for protein folding and quality control in the endoplasmic reticulum. *Biochim Biophys Acta Mol Cell Res*. 2012;1823(3):774-787.
47. Sasai M, Linehan MM, Iwasaki A. Bifurcation of Toll-like receptor 9 signaling by adaptor protein 3. *Science*. 2010;329(5998):1530-1534.
48. Stawowczyk M, Van Scoy S, Kumar KP, Reich NC. The interferon stimulated gene 54 promotes apoptosis. *J Biol Chem*. 2011;286(9):7257-7266.
49. Bird PI. Serpins and regulation of cell death. *Apoptosis: Mechanisms and Role in Disease*: Springer. 1998;63-89.
50. Irmiler M, Steiner V, Ruegg C, Wajant H, Tschopp J. Caspase-induced inactivation of the anti-apoptotic TRAF1 during Fas ligand-mediated apoptosis. *FEBS Lett*. 2000;468(2-3):129-133.
51. Seaborne RA, Strauss J, Cocks M, et al. Human skeletal muscle possesses an epigenetic memory of hypertrophy. *Sci Rep*. 2018;8(1):1898.
52. Suchi M, Mizuno H, Kawai Y, et al. Molecular cloning of the human UMP synthase gene and characterization of point mutations in two hereditary orotic aciduria families. *Am J Hum Genet*. 1997;60(3):525-539.
53. Gibson KM, Hoffmann CF, Hodson AK, Bottiglieri T, Jakobs C. 4-Hydroxybutyric acid and the clinical phenotype of succinic semialdehyde dehydrogenase deficiency, an inborn error of GABA metabolism. *Neuropediatrics*. 1998;29(01):14-22.
54. Momb J, Lewandowski JP, Bryant JD, et al. Deletion of Mthfd1l causes embryonic lethality and neural tube and craniofacial defects in mice. *Proc Natl Acad Sci USA*. 2013;110(2):549.
55. Shin M, Bryant JD, Momb J, Appling DR. Mitochondrial MTHFD2L is a dual redox cofactor-specific methylenetetrahydrofolate dehydrogenase/methenyltetrahydrofolate cyclohydrolase expressed in both adult and embryonic tissues. *J Biol Chem*. 2014;289(22):15507-15517.

## SUPPORTING INFORMATION

Additional supporting information may be found online in the Supporting Information section.

Fig S1

Fig S2-Slide1

Fig S2-Slide2

Fig S2-Slide3

Fig S2-Slide4

Supplementary Material

**How to cite this article:** Kohlschmidt N, Elbracht M, Czech A, et al. Molecular pathophysiology of human MICU1 deficiency. *Neuropathol Appl Neurobiol*. 2021;47:840-855. <https://doi.org/10.1111/nan.12694>